Optimal Gait Design for a Soft Quadruped Robot via Multi-fidelity Bayesian Optimization

Kaige Tan[a], Xuezhi Niu[a], Qinglei Ji[a], Lei Feng[a,*], Martin Törngren[a]

[a]*Department of Engineering Design, KTH Royal Institute of Technology, Stockholm 10044, Sweden*

Abstract

This study focuses on the locomotion capability improvement in a tendon-driven soft quadruped robot through an online adaptive learning approach. Leveraging the inverse kinematics model of the soft quadruped robot, we employ a central pattern generator to design a parametric gait pattern, and use Bayesian optimization (BO) to find the optimal parameters. Further, to address the challenges of modeling discrepancies, we implement a multi-fidelity BO approach, combining data from both simulation and physical experiments throughout training and optimization. This strategy enables the adaptive refinement of the gait pattern and ensures a smooth transition from simulation to real-world deployment for the controller. Moreover, we integrate a computational task off-loading architecture by edge computing, which reduces the onboard computational and memory overhead, to improve real-time control performance and facilitate an effective online learning process. The proposed approach successfully achieves optimal walking gait design for physical deployment with high efficiency, effectively addressing challenges related to the reality gap in soft robotics.

Keywords: Soft quadruped robot, Reality gap, Multi-fidelity Bayesian optimization, Edge computing.

1. Introduction

Soft robotics, utilizing compliant materials and structures as actuators, is gaining prominence for creating adaptive and resilient robotic systems, particularly in soft quadruped robots with legged locomotion [1]. In contrast to their rigid counterparts, soft quadruped robots are featured with compliant materials and soft actuators, emulating the flexibility of biological tissue. Actuated by pneumatic pressure [2, 3], electric voltage [4, 5], and magnetic fields [6, 7], soft robots demonstrate resilience to diverse working conditions, enhance safety in human-machine interactions, and effectively absorb external disturbances through their inherent elasticity [8].

While soft actuators facilitate intricate deformations for complex locomotion, effective gait design is the necessity of exploiting the full walking potential of soft robots [9]. The challenges arise from the soft robots' modeling complexity under environmental interactions and the inherent difficulty of maintaining consistent actuation force and precision for soft actuators [10], a concern not shared by their rigid counterparts.

To resolve the above challenge, tendon-driven soft actuators (TSAs) are utilized for actuation, where the actuators' bending and compression motions are synchronized to improve the walking performance of the robot [11, 9, 8, 12]. Prior research primarily focuses on predefined gait trajectories [9, 8] or model-based control designs for gait optimization [11, 12]. However, the gait trajectory is either not optimized or only optimized through Finite Element Analysis (FEA) [13, 14] which fails to achieve good time efficiency. Therefore, a research gap persists for advanced gait exploration in developing an optimal gait pattern for TSA-type soft robots.

To create adaptive and efficient locomotion patterns, many state-of-the-art techniques provide sophisticated solutions tailored for rigid quadruped robots, including reinforcement learning [15, 16, 17], Central Pattern Generators (CPGs) [18, 19, 20], and model predictive control [21, 22, 23]. A comprehensive overview of the relevant approaches can be found in the work of Taheri et al. [24]. Specifically, artificial CPGs, which contain limited cycles with repeating patterns for gait synchronization, have been proposed as a robust approach to enhancing gait stability. CPGs can be designed by modeling the behavior of neuron cells as neuron oscil-

---

lators [25]. Alternatively, another type of CPG is designed based on dynamic systems, e.g., Hopf oscillators [26] and van-der-Pol oscillators [27]. The oscillators can generate rhythmic signals in the form of trajectories and represent the stance-swing sequence of the legs with continuous states, making them well-suited for modeling gait patterns in soft quadruped robots.

Essentially, these oscillator models often contain tuning parameters, which require a well-designed method for users to properly choose their values. There are two major considerations for achieving optimal performance when applying the parametric locomotion design framework to the soft quadruped robots:

- **Uncertain parameter optimization**: Owing to the intrinsic nonlinear and time-variant properties of the soft material, the dynamics of the soft actuators is subject to significant uncertainty. Traditional deterministic functions and optimization methods lack robustness when applied to the soft robot gait design.

- **Modeling error compensation**: Precisely modeling the dynamics of soft materials is challenging due to their compliant nature. Consequently, it is imperative to address the discrepancies between simulation and real-world performance of soft robots. The inherent complexities of soft robotic systems pose challenges for simulators to accurately replicate them. Therefore, it becomes crucial to devise strategies for reducing this modeling error during physical deployment.

To address the first challenge, the implicit relationship between the model parameters and the objective function is generally treated as a stochastic black-box model, where optimal parameter values can be determined through black-box optimization methodologies. Solving black-box optimization via soft computing has proven effective in various robotics applications. Notably, algorithms such as Bayesian Optimization (BO) [28], Particle Swarm Optimization (PSO) [29], and Evolutionary Algorithms (EA) [30] have been extensively employed. Among them, BO has the advantage of considering probabilistic objective functions and using efficient sampling to achieve fast convergence. Thus, given the parametric-based gait pattern, BO stands out as an ideal choice for systematically tuning uncertain parameters, thereby unlocking the potential of the robot's gait with high exploration efficiency.

The second challenge stems from the inevitable discrepancies between the simulation model and the real robot, owing to noise, perturbations, and modeling errors. This disparity, often referred to as the *reality gap*, leads to discrepancies within a simulator-aided framework, necessitating adjustments to the optimal solution identified in the simulation environment through physical experiments [31]. When developing a data-driven controller, abundant synthetic training data can be obtained from the simulator, but the data contain unavoidable errors compared to data derived from real robots. Moreover, while measurement data from real robots are of high quality, obtaining them in large quantities is challenging due to the need for human supervision and experiment resets, resulting in a slow and costly process [15]. To address this challenge, our method mixes the two types of data in a single learning algorithm to alleviate the reality gap between simulation and physical robots. Specifically, we focus on the BO method and propose a *multi-fidelity BO* (MFBO) approach to achieve efficient sim-to-real adaptation of the optimal points between the model and the robot. Consequently, the optimal walking pattern learned from simulations can be efficiently adapted to the physical robot through online learning in the real world.

MFBO extends the traditional BO framework to incorporate information from diverse sources with different fidelity levels. While BO typically relies on a Gaussian Process (GP) model as a surrogate to represent objective function evaluations, it is limited by a scalar output for a single model characterization. To address this limitation, either separate GPs are used for distinct models [32], or an error function is trained to delineate the difference among different models [33]. Additionally, the multi-task GP (MTGP) method [34, 35] has been introduced to naturally manage multiple coupled outputs, capturing complex data dependencies arising from various sources.

Incorporating MTGP into the BO framework gives rise to the MFBO method, which facilitates accelerated model training across different data sources. Recently, MFBO has found applications in various research domains, e.g., hyper-parameter optimization [36], process optimization [37], and safe controller design [38]. However, its potential for modeling error compensation in robotics systems, particularly in adaptive controller design, remains underexplored.

Similar to this paper, Lan et al. [18] integrate BO and CPG for the robot's optimal gait pattern generation. Although they identify the reality gap during the physical testing, they do not propose a method to adapt the gait pattern to the physical robot. The shortcoming prompts our exploration of the MFBO approach to the efficient adaptation of the gait controller learned from simulations to the physical robot. The adaptation proce-

dure is performed through online learning with the real robot, which combines both previously obtained simulation data and the online generated real-world data to obtain a better gait controller for the physical robot. It is worth noting prior studies do not distinguish the terms *multi-fidelity* and *multi-task* within the same BO framework. We adopt the term *multi-fidelity* in the sequel to maintain clarity and underscore its relevance within the context of sim-to-real transfer scenarios [39].

Moreover, the complexities of online MFBO training and the challenges associated with CPG gait generation pose difficulties for achieving real-time control on the robot's onboard computation system. Recently, the integration of edge computing has emerged as a promising solution to enhance robotic system performance [40, 41]. Computational task off-loading becomes instrumental in load balancing [42] and optimizing resource utilization [43]. Furthermore, compared to task off-loading to the public cloud, the integration of edge computing allows for data processing closer to the source with less latency, ensures real-time computational task completion [10], and improves the system responsiveness [44]. Therefore, our study leverages the computational off-loading enabled by edge computing to improve the real-time control performance for the soft quadruped robot gait design.

In summary, the contributions of our article are as follows.

1. A gait generator is devised for the soft quadruped robot with CPG-based modeling. The utilization of a parametric formulation enhances the adaptability and flexibility of gait pattern design.

2. The computation of the optimal gait pattern parameters is formulated as a stochastic black-box optimization problem, which is solved using the MFBO approach. Our approach effectively mitigates the reality gap and achieves a rapid transition from sim-to-real adaptation.

3. An online learning architecture is designed based on an edge computing framework. Complex MFBO optimization and training tasks are performed at the edge server. Computational task off-loading, facilitated by 5G communication, allows for real-time adaptive parameter optimization and fast deployment.

The rest of this article is organized as follows. Followed by the preliminaries in Sec. 2, Sec. 3 introduces the soft quadruped robot under study and CPG-based gait pattern model design. Then, the formulated parameter optimization problem is solved by MFBO in Sec. 4.

Sec. 5 describes the hardware implementation and the experiment setup. Sec. 6 shows the evaluation and results of the approach. Finally, Sec. 7 concludes this article.

2. Preliminaries

2.1. Gaussian Processes Model

A GP model represents a stochastic function $g : \mathcal{P} \to \mathbb{R}$, where $\mathcal{P}$ is a subset of $\mathbb{R}^n$. A GP model is specified by its mean and covariance functions, i.e., $m : \mathcal{P} \to \mathbb{R}$ and $k : \mathcal{P} \times \mathcal{P} \to \mathbb{R}$. For a point $\mathbf{p} \in \mathcal{P}$, $g(\mathbf{p}) \sim \mathcal{GP}(m(\mathbf{p}), k(\mathbf{p}, \mathbf{p}))$ is a random value with the Gaussian distribution whose mean is $m(\mathbf{p}) = \mathbb{E}[g(\mathbf{p})] \in \mathbb{R}$ and variance is $k(\mathbf{p}, \mathbf{p})$. For any two points $\mathbf{p}, \mathbf{p}' \in \mathcal{P}$, the covariance is defined by $k(\mathbf{p}, \mathbf{p}') = \mathbb{E}[(g(\mathbf{p}) - m(\mathbf{p}))(g(\mathbf{p}') - m(\mathbf{p}'))] \in \mathbb{R}_+$. The covariance function defines the relationships between data points in the input space, which is characterized by the hyperparameters $\boldsymbol{\lambda}$. They impact the shape of regression functions and can be optimally defined by log marginal likelihood. With a training data set $\mathcal{T} = \{[\mathbf{p}_i, v_i], i = 1, \dots, n\}$ of n training samples $\mathbf{P} = [\mathbf{p}_1, \dots, \mathbf{p}_n]$ and their corresponding outputs $\mathbf{v} = [v_1, \dots, v_n]$, the optimal values $\boldsymbol{\lambda}^*$ can be acquired by maximizing the likelihood of the observed outputs. Based on that, the GP model can be used to predict the function value v' of a test point $\mathbf{p}'$, yielding

$$p(v' \mid \mathbf{p}', \boldsymbol{\lambda}^*, \mathcal{T}) = \mathcal{N}\left(\mu_{\mathbf{p}'}, \sigma_{\mathbf{p}'}\right), \tag{1}$$

and

$$\begin{aligned} \mu_{\mathbf{p}'} &= k(\mathbf{P}, \mathbf{p}')^\top K_{\mathbf{P}}^{-1} \mathbf{v}^\top, \\ \sigma_{\mathbf{p}'} &= k(\mathbf{p}', \mathbf{p}') - k(\mathbf{P}, \mathbf{p}')^\top K_{\mathbf{P}}^{-1} k(\mathbf{P}, \mathbf{p}'), \end{aligned} \tag{2}$$

where $\mu_{\mathbf{p}'}$ and $\sigma_{\mathbf{p}'}$ are the mean and variance of v'. $K_{\mathbf{P}}$ is the symmetric and positive semi-definite $n \times n$ covariance matrix and $K_{\mathbf{P}}(i, j) = k(\mathbf{p}_i, \mathbf{p}_j)$. $k(\mathbf{P}, \mathbf{p}')$ is an $n \times 1$ vector, and each entry denotes the kernel function value between $\mathbf{p}_i \in \mathbf{P}$ and $\mathbf{p}'$. The values of $k(\cdot, \cdot)$ and $K_{\mathbf{P}}$ in (2) depend on $\boldsymbol{\lambda}^*$.

2.2. Bayesian Optimization

Bayesian optimization (BO) is an effective optimization technique for black-box optimization. The method employs a data fitting surrogate model $g(\cdot)$ to approximate the unknown objective function $J(\cdot)$. The selection of the surrogate model is crucial for accuracy and efficiency [45]. Popular surrogate models include GP, random forest (RF), piece-wise linear (PL), and etc.. The GP model is often preferred for two primary reasons: 1) its ability to quantify uncertainty in predictions, and 2)

its adaptation for mitigation of the reality gap in MFBO. Comparisons of different surrogate models for BO are presented later in Sec. 6.3.

Based on the training data set and the GP model hyperparameters, Bayesian optimization maximizes an acquisition function $a(\cdot)$ to determine the next most promising point to evaluate in the search for global optimality of $J(\cdot)$, i.e., $\mathbf{p}_{\text{next}} = \text{argmax}_{\mathbf{p}} \, a(\mathbf{p} \mid \mathcal{T}, \boldsymbol{\lambda})$. After evaluating the newly generated point, i.e., obtaining $J(\mathbf{p}_{\text{next}})$, the GP model will also be updated based on the new observation. The iterative cycle continues until predetermined stopping conditions are met, such as a predetermined number of iterations or convergence criteria. If the stopping conditions are proper, the iteration converges to the optimal solution.

Many types of acquisition functions $a(\cdot)$ have been proposed, e.g., expected improvement criterion (EI), Probability of Improvement (PI), and GP upper confidence bounds (GP-UCB). EI has proved its superiority over PI, and it does not require the tuning parameter as in GP-UCB [46]. Thus, EI is adopted in this study, which maximizes the expected improvement over the current best J^*, i.e.,

$$a_{\text{EI}}(\mathbf{p} \mid \mathcal{T}, \boldsymbol{\lambda}) = \mathbb{E}(\max[0, g(\mathbf{p}) - J^*] \mid \mathcal{T}, \boldsymbol{\lambda}). \quad (3)$$

It has a closed form under the GP surrogate model, i.e.,

$$\begin{aligned} a_{\text{EI}}(\mathbf{p} \mid \mathcal{T}, \boldsymbol{\lambda}) &= \sqrt{\sigma_{\mathbf{p}}}[\gamma(\mathbf{p})\Phi(\gamma(\mathbf{p})) + \phi(\mathbf{p})], \\ \gamma(\mathbf{p}) &= (\mu_{\mathbf{p}} - J^*) / \sqrt{\sigma_{\mathbf{p}}}, \end{aligned} \quad (4)$$

where $\mu_{\mathbf{p}}$ and $\sigma_{\mathbf{p}}$ are obtained from (2). $\phi(\cdot)$ denotes the standard normal density function, and $\Phi(\cdot)$ denotes the cumulative distribution function of the standard normal distribution.

2.3. Hopf Oscillator

As a method to model the artificial CPG, Hopf oscillator produces various harmonic output patterns, and has a clear correlation with the applied coefficients. It can be denoted by the oscillator state $\mathbf{o}$, which takes the form of the nonlinear differential equations:

$$\dot{\mathbf{o}} = f_{\text{h}}(\mathbf{o}) + \mathbf{q} = \begin{bmatrix} k(A^2 - o_1^2 - o_2^2)o_1 - 2\pi f o_2 \\ k(A^2 - o_1^2 - o_2^2)o_2 + 2\pi f o_1 \end{bmatrix} + \begin{bmatrix} q_1 \\ q_2 \end{bmatrix}, \quad (5)$$

where $\mathbf{o} = [o_1, o_2]^\top$ is the Hopf oscillator state vector. $\mathbf{q} = [q_1, q_2]^\top$ is a design coupling vector to coordinate different oscillators. The formulas for q_1 and q_2 are defined later in (12). A, f, and k are design parameters that determine the amplitude of the steady-state oscillation, oscillation frequency, and the speed of convergence, re-

spectively. Given the design parameters and a non-zero initial state, a harmonic pattern will be generated from the oscillator represented by o_1 and o_2. Note that $\mathbf{o}$ is time-dependent; however, for the sake of simplicity, we shall include the argument of time in the expression only when essential.

In addition, a dynamic modulation of frequency is introduced to generalize the oscillator formulation. It is realized by employing a varying frequency influenced by the state of oscillator, thus achieving a non-harmonic pattern. Given the shape ratio α and time constant τ, the constant frequency f in (5) can be adjusted to yield a frequency f_a, where

$$f_a(o_2) = \frac{f}{2\alpha} + \frac{(2\alpha - 1)f}{2\alpha(1 - \alpha)(1 + e^{-\tau o_2})}. \quad (6)$$

Note that the period T of the oscillator in (6) is still determined by f (i.e., $T = 1/f$), and the harmonic pattern is a special case of (6) when $\alpha = 0.5$. When $\alpha \neq 0.5$, the frequency f_a changes monotonically in each oscillation period. We direct the interested reader to reference [47] for the comprehensive analysis on Hopf oscillators. Note that f_a is a state-dependent variable of o_2. As a result, the other state, i.e., o_1, becomes the exclusive determinant of the fundamental gait trajectory, and its value serves as the output of the Hopf oscillator in the sequel.

3. Parametric Gait Pattern Model

3.1. Inverse Kinematics: Task Level to Motor Level

Our previous works [5, 8] introduce the design and fabraction of a soft quadruped robot characterized by its innovative utilization of four TSAs. Figure 1(a) provides a visual representation of the robot, illustrating key states of robot such as roll (θ_x), pitch (θ_y), yaw (θ_z), translational velocities along three axes (v_x, v_y, v_z), and the normal contact forces on each foot ($f_{nFL}, f_{nFR}, f_{nRL}, f_{nRR}$). The defining characteristic of the TSAs is the cable-driven mechanism, which enables seamless and continuous bending and twisting along its entire length. The cables, also referred to as tendons, guide the deformation of soft materials, facilitating precise movement to designated positions. Each leg of the robot is actuated by three cables, which are driven by servo motors, resulting in the generation of tendon displacement denoted as $\mathbf{x}_{\text{ten}} = [x_A, x_B, x_C]^\top$, as illustrated in Figure 1(b). The state of each soft leg is characterized by

$$\mathbf{s} = [\alpha_{\text{b}}, \alpha_{\text{r}}, z_{\text{l}}]^\top, \quad (7)$$
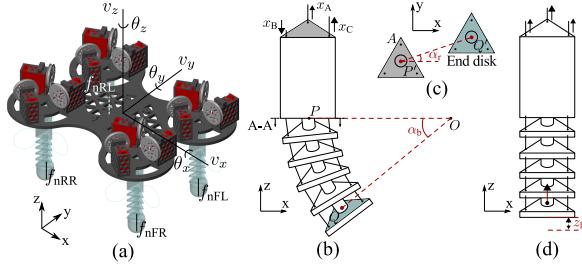
4

Figure 1: Overview of the soft robot and its Tendon-driven Soft Actuator (TSA): (a) Rendered robot with key states. (b) Structure of TSA: rigid upper thigh and bendable lower section with α_b. (c) Top view of bent TSA with α_r. (d) TSA compression via equal tendon pull with z_l.

as shown in Figure 1(b)-(d). The mapping of a feasible $\mathbf{s}$ into the corresponding tendon displacement $\mathbf{x}_{\text{ten}}$ is investigated in the previous work [8] as the following function.

$$\mathbf{x}_{\text{ten}} = g_{\text{inv}}(\mathbf{s}) = f_{\text{inv}}([\alpha_b, \alpha_r]^\top) + \mathbf{1}z_l, \qquad (8)$$

where $f_{\text{inv}} : \mathbb{R}^2 \to \mathbb{R}^3$ is derived through geometric analysis, and

$$
\begin{aligned}
x_A &= R_d \alpha_b \cos(\alpha_r), \\
x_B &= R_d \alpha_b \cos(\alpha_r + \frac{2\pi}{3}), \\
x_C &= R_d \alpha_b \cos(\alpha_r + \frac{4\pi}{3}).
\end{aligned}
\qquad (9)
$$

R_d is the radius of the circle formed by the three guiding holes on a disk. $\mathbf{x}_{\text{ten}}$, as the tendon displacement, is further used as the motor reference for the low-level position control. The synchronization of the designed trajectory on $\mathbf{s}$ and $\mathbf{x}_{\text{ten}}$ will lead to a gait pattern of the robot on the task level.

Moreover, a simulation environment utilizing MAT-LAB Simulink Multibody blocks is developed [5, 8], providing a digital emulation of the real robot. The plant model within the simulator exhibits a high level of modeling accuracy corresponding to the physical world, which supports and prompts the design of motion controllers. In addition, note that various terms, e.g., *real robot*, *physical robot*, and *real-world robot*, are interchangeable in what follows, all referring to the entity existing physically within the tangible environment, as opposed to the simulated robotic platform employed.

3.2. Gait Pattern Generation

In the previous study [8], the temporal trajectory of $\mathbf{s}$ is characterized by an ad hoc design approach, which

is non-optimal in terms of robot walking speed and efficiency. State-of-the-art research usually identifies the walking of a quadruped robot by rhythmic patterns; hence, the nonlinear oscillator can be used as an ideal option to model a rhythmic movement in a formalized and parametric way. Therefore, to improve the gait design, we employ nonlinear oscillators to model the rhythmic movement of the actuator states.

Using the inverse kinematic model in (8), this study applies the Hopf oscillator as a fundamental pattern generator for the robot locomotion pattern design. Following the notation in Sec. 2.3, we denote by $\mathbf{o}_i$ the oscillator state of cycle behavior $\mathbf{s}_i$ of leg-i, $i \in \mathcal{I} = \{1, 2, 3, 4\}$. To unify the cycle behavior of each leg and promote their coordination, we assume the oscillator motion of legs $\mathbf{o}_i$ is originated from a primitive oscillator $\mathbf{o}$ based on (5)-(6).

Nevertheless, the Hopf oscillators of each leg are yet coordinated to shape gait patterns and generate motor trajectory references. To realize it, coupling term $\mathbf{q}_i$ is designed to generate coupled oscillator $\mathbf{o}_i$ of each leg from the primitive oscillator $\mathbf{o}$. The distinct behavior of each leg is represented by a phase difference

$$\boldsymbol{\theta} = [\theta_1, \theta_2, \theta_3, \theta_4]. \qquad (10)$$

Thus, the rhythmic trajectory of each leg is defined by

$$\mathbf{o}_i(t) = \mathbf{o}(t - \Delta t_i), \ \Delta t_i = \theta_i/(2\pi), \ i \in \mathcal{I}. \qquad (11)$$

This study considers that the oscillator $\mathbf{o}_i$ is coupled and perturbed by the primitive oscillator $\mathbf{o}$. Given the target phase difference $\theta_i = \boldsymbol{\theta}[i]$, the coupling term of the i-th oscillator is calculated by

$$\mathbf{q}_i = \begin{bmatrix} q_1 \\ q_2 \end{bmatrix}_i = \begin{bmatrix} 0 \\ \varepsilon(o_1 \sin \theta_i + o_2 \cos \theta_i) \end{bmatrix}, \qquad (12)$$

where $\varepsilon > 0$ denotes the coupling strength. By designing the values of $\boldsymbol{\theta}$, the oscillator of each leg $\mathbf{o}_i$ is defined. Thus, actuators of legs can be synchronized to compose different locomotive patterns, e.g., trotting, galloping, depending on the values of $\boldsymbol{\theta}$. Figure 2 illustrates an example of the non-harmonic oscillator response with varying frequencies, where $\mathbf{o}'$ is generated from $\mathbf{o}$. $o_1 = \mathbf{o}[1]$ and $o_1' = \mathbf{o}'[1]$ defined in (5) are used as the output of the oscillator. In the figure, two coupled oscillators have the same pattern but different phases. $\Delta t'$ is defined by $\theta' = \pi/2$.

Subsequently, the derivation of $\mathbf{o}_i$ is applied to the design of $\mathbf{s}_i$. Recap that in $\mathbf{s}_i$, the rotational angle $\alpha_{r,i}$ of the leg influences the movement direction of the quadruped robot. Especially, the prior study [8] has demonstrated
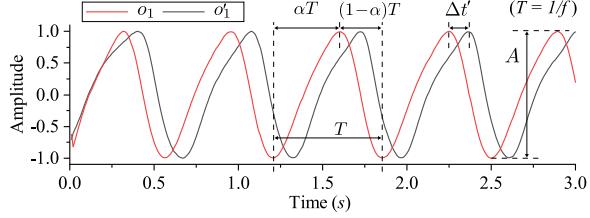
Figure 2: The non-harmonic oscillator response with varying frequencies. In this example, the initial state is randomized, and $[A, f, \alpha, \tau, k, \epsilon, \Delta t'] = [1, 1.33, 0.75, 1, 1000, 5, 0.25]$.

that the direction of movement θ_z corresponds to the angular rotations of the legs when all four legs exhibit uniform values, i.e., $\forall i \in \mathcal{I}, \alpha_{r,i} = \theta_z$. Therefore, given a reference trajectory with the direction of movement θ_{ref}, we can simplify the problem by setting $\alpha_{r,i} = \theta_{\text{ref}}$.

Thus, the cyclic behavior $\mathbf{s}_i$ is essentially defined by $\alpha_{b,i}$ and $z_{1,i}$, which determine the trajectory and amplitude of the foot pattern. Based on the previous analysis, the rhythmic behaviors can be effectively characterized by the state output $o_{1,i}$ originating from the Hopf oscillator. Note that, for the sake of simplifying the design process and limiting the parameter space, we consider $\alpha_{b,i}$ and $z_{1,i}$ as interrelated, and both are characterized by the same oscillator output $o_{1,i}$ but with distinct phases and gains, i.e.,

$$\alpha_{b,i}(t) = o_{1,i}(t), \quad \frac{\alpha_{b,i}(t)}{A_{\alpha_b}} = \frac{z_{1,i}(t - \varphi)}{A_{z_1}}, \quad (13)$$

where $\varphi \in [0, T]$ is a design parameter, which represents the delay between the patterns of $\alpha_{b,i}$ and $z_{1,i}$. This delay parameter allows for fine-tuning the synchronization between these two critical components in the gait pattern generation. A_{α_b} and A_{z_1} denote the amplitudes for α_b and z_1, respectively. We consider that both trajectories share the same frequency f and shape ratio α in order to generate the rhythmic pattern.

3.3. Optimization Problem Formulation

Based on the above analysis, the coordinated cycle behavior of each leg $\mathbf{s}_i$ can be defined by the oscillator state $\mathbf{o}_i$, the correlated phase difference φ, and the reference direction θ_{ref}, and $\mathbf{o}_i$ is further influenced by the base oscillator $\mathbf{o}$ and coupling term $\mathbf{q}_i$ through (11)-(13). Thus,

$$\mathbf{s}_i = f_{\text{CPG}} \left(\mathbf{o}, \mathbf{q}_i, \varphi, \theta_{\text{ref}} \right). \quad (14)$$

Eq. (14) provides a formulation of the rhythmic and coordinated gait pattern enabled by Hopf oscillator. This formulation enables the generation of coordinated leg

movements in response to the specified reference direction and desired phase synchronization. Accordingly, the references $\mathbf{x}_{\text{ten}}$ for the 12 motors can be calculated from $\mathbf{s}_i$ through (8). If the reference trajectories $\mathbf{x}_{\text{ten}}$ are provided to the robot's simulation model, the simulation outcomes can be analyzed to evaluate the quality of the gait pattern.

Generally, a gait of the leg robot is determined by three factors: stride, duty cycle, and phase factor. In our model, the phase factor is controlled by $\boldsymbol{\theta}$ in (10) for the leg synchronization, and the other two are derived from the trajectory of $\mathbf{s}_i$ based on (14). Note that in (14), given the initial state $\mathbf{o}(t_0)$, $\mathbf{o}$ is determined by parameters $A_{\alpha_b}, A_{z_1}, f, \alpha, \tau, k$, and $\mathbf{q}_i$ is computed based on ε, θ_i. Among those, τ, k, ε control the stability and convergence of the oscillators but will not influence their steady-state behaviors; thus, those parameters are irrelevant to the gait design, which are regarded as constant and predefined in the design phase.

Therefore, besides θ_{ref} and $\boldsymbol{\theta}$ that explicitly define the robot walking direction and phase factor (which can be pre-designed), the other walking properties are determined by $\mathbf{o}$, $\mathbf{q}_i$ and φ. To summarize, based on (5), (6), and (13), the choice of parameters in the vector $\mathbf{p} = [A_{\alpha_b}, A_{z_1}, f, \alpha, \varphi]^\top \in \mathbb{R}^5$ significantly influences the stride and duty cycle of the gait, thus influences various aspects of the robot's walking properties, e.g., walking speed, Cost of Transport (COT), terrain clearance, and stride length.

By designing and optimizing the associated design parameters in $\mathbf{p}$, the parametric formulation of the gait pattern $\mathbf{s}_i$ enables the shaping of an optimal robot walking pattern. Considering the inverse kinematic mapping in Sec. 3.1, the relationship between $\mathbf{p}$ and the objective function set up an end-to-end design from motor actuation commands to the robot walking task-level control. Specifically, as an intuitive representative of the interested properties, this study defines the objective function by maximizing the robot walking speed v. Nevertheless, the proposed approach can also be applied and analyzed for the other walking properties as mentioned before. Within our CPG-based parametric gait pattern framework, we assume that a set of parameter $\mathbf{p}$ will lead to a stabilized robot walking speed v.

Owing to the lack of a known mathematical form, the evaluation of the walking speed v for a candidate parameter vector $\mathbf{p}$ is based on the simulation results of the robot model. If we view the simulated robot as a black-box model, this parameter design problem becomes a black-box optimization problem. Given the unknown mapping function $J : \mathbb{R}^5 \rightarrow \mathbb{R}$ with the design space $\mathcal{P} = \{\mathbf{p} \in \mathbb{R}^5 : \underline{p_i} \leq \mathbf{p}_i \leq \overline{p_i}\}$, where $\underline{p_i}$ and $\overline{p_i}$ denote the

lower and upper bounds for each element, the optimal walking speed can be identified through

$$v^* = \max_{\mathbf{p} \in \mathcal{P}} \quad J(\mathbf{p}), \qquad (15)$$

This black-box optimization problem is solved by the Baysian optimization method introduced in Section 2.2.

4. Adaptive Optimal Gait Design by Multi-fidelity Bayesian Optimization

4.1. Reality Gap from the Digital Replica

The optimization problem in (15) can be effectively addressed by BO method, which employs a GP model to approximate the unknown function $J(\cdot)$. BO iteratively selects candidate points for evaluation and uses the gained information to guide the search towards the optimal solution. However, implementing this process in a physical robotics setup is typically troublesome, since each direct evaluation of $J(\cdot)$ on the robot can be resource-intensive, potentially causing wear and taking a long time to execute.

To minimize the number of physical evaluation queries and optimize the parameters efficiently, we leverage a simulator model of the quadruped robot [5]. This simulator model serves as a digital replica of the real robot, providing evaluation results with reduced effort and time compared to physical evaluations. Consequently, the optimal combination of parameters can be identified through the optimization of the evaluation results obtained via simulation, making the process more cost-effective.

Nonetheless, it is crucial to account for the unavoidable discrepancies between the simulator and the real robot, and the non-negligible reality gap is demonstrated in our previous experiments [5]. As an alternative, the optimal points can be identified directly from the physical robot with the BO framework; however, as previously discussed, $J(\cdot)$ is expensive to evaluate in the physical experiments, resulting in increased workload and difficulty in data collection during the iterative process.

To ensure that optimal performance can be achieved in the physical environment, we introduce an MFBO approach based on the BO framework for domain adaptation and online training. It facilitates the transfer of knowledge from simulation to reality during parameter optimization. Thus, the optimal solution is adapted and evolved efficiently from model-based optimization to the physical implementation.

4.2. Multi-fidelity Bayesian Optimization

Both the simulator and the physical robot can be modeled as two different GP models with the same input and output states. Thus, in the BO framework, the two GP models for the same subject are correlated, and their inter-model correlations can be exploited for efficient learning. To achieve this, we employ the MTGP model to substitute the single output GP model. This substitution allows us to leverage multiple outputs that capture diverse behaviors of various plant models. We create a tuple $\langle \mathbf{p}_i, j \rangle$ by augmenting the input sample with the fidelity identifiers j, where $j \in \{1, 2\}$ denotes the simulator and physical environment. To reflect the similarity constraint, we define a new covariance function over the identifier by $k_f(j, j')$. With *intrinsic model of coregionalization* [48], we reconstruct the kernel function with

$$\tilde{k}(\langle \mathbf{p}_i, j \rangle, \langle \mathbf{p}_{i'}, j' \rangle) = k_f(j, j')k(\mathbf{p}_i, \mathbf{p}_{i'}), \qquad (16)$$

where $k(\cdot, \cdot)$ is defined in Sec. 2.1. $k_f(\cdot, \cdot)$ is the additional covariance function representing the correlation over models, which takes the model labels as input.

For the training input set $\mathbf{P}$ with n samples, we first assume the complete set of evaluation results on $J(\cdot)$ is available for both fidelity levels with $\tilde{\mathbf{v}} = [\mathbf{v}^1, \mathbf{v}^2]$, where $\mathbf{v}^j = [v_1^j, \ldots, v_n^j], j \in \{1, 2\}$. Based on (16), the covariance matrix $\tilde{K}$ for the data from both fidelity levels can be obtained with

$$\tilde{K} = K_f \otimes K_{\mathbf{P}}, \qquad (17)$$

where $\otimes$ denotes Kronecker product, $K_f \in \mathbb{R}^{2 \times 2}$ is a symmetric matrix whose diagonal entries represent the inner-task relationship with themselves, and the other elements describe the correlations of different fidelity levels. Note that if all the off-diagonal entries are zeros, K_f becomes an identity matrix, which means all the underlying data sources are independent.

The parameters for an MTGP model include λ and K_f. We denote them collectively as $\Lambda = \begin{bmatrix} \lambda & \text{vec}(K_f) \end{bmatrix}^\top$, where $\text{vec}(\cdot)$ denotes the column vectorization of a matrix. An MTGP model is optimized similarly to that in Sec. 2.1 by maximizing the marginal likelihood for Λ. We leave out the derivation of hyperparameter learning for simplicity. Accordingly, the prediction of the test point $\langle \mathbf{p}', j' \rangle$ can be achieved by calculating the conditional probability with

$$p(v' \mid \langle \mathbf{p}', j' \rangle, \Lambda^*, \mathbf{P}, \tilde{\mathbf{v}}) = \mathcal{N}(\mu_{\mathbf{p}'}, \sigma_{\mathbf{p}'}), \qquad (18)$$

and

$$\mu_{\mathbf{p}'} = \tilde{k}(\mathbf{P}, \langle \mathbf{p}', j' \rangle)^\top \tilde{K}^{-1} \tilde{\mathbf{v}}^\top,$$

$$\sigma_{\mathbf{p}'} = \tilde{k}(\langle \mathbf{p}', j' \rangle, \langle \mathbf{p}', j' \rangle) - \tilde{k}(\mathbf{P}, \langle \mathbf{p}', j' \rangle)^\top \tilde{K}^{-1} \tilde{k}(\mathbf{P}, \langle \mathbf{p}', j' \rangle), \quad (19)$$

where $\tilde{k}(\mathbf{P}, \langle \mathbf{p}', j' \rangle)$ denotes the kernel vector in the MTGP model for the test point tuple $\langle \mathbf{p}', j' \rangle$, and

$$\tilde{k}(\mathbf{P}, \langle \mathbf{p}', j' \rangle) = (K_f)_{j'} \otimes k(\mathbf{P}, \mathbf{p}'). \quad (20)$$

$(K_f)_{j'}$ is a 2×1 vector where $(\cdot)_{j'}$ selects the j'-th column of the matrix K_f. Recall that $k(\mathbf{P}, \mathbf{p}')$ is an $n \times 1$ vector, which leads to the size of kernel vector $\tilde{k}(\mathbf{P}, \langle \mathbf{p}', j' \rangle)$ becoming $2n \times 1$. It evaluates the kernel value of the test input with respect to all training data points from both fidelity models. To differentiate the single output GP model in (1)-(2), we denote by $\tilde{g}(\langle \mathbf{p}, j \rangle)$ the MTGP model.

Built upon the MTGP model, the MFBO process can be updated accordingly. To be specific, in (3)-(4), $g(\mathbf{p})$ is evaluated instead by $\tilde{g}(\langle \mathbf{p}, j \rangle)$ through (16)-(20). And the generated point by maximizing the acquisition function corresponds to an optimal candidate point for the physical robot. By performing the MFBO iterations, the precision of the MTGP is enhanced by incorporating additional data from the physical measurement. Consequently, this process facilitates the identification of the optimal point for the physical robot, thereby enabling the achievement of domain adaptation across models efficiently.

Remark 1. Owing to the expression simplicity, we utilize the *isotopic data* [48] for the derivation in (17)-(20), where the outputs $\tilde{\mathbf{v}}$ are assumed fully observable for both simulator and physical robot based on the input set $\mathbf{P}$. However, in practical implementation, the collected data $\tilde{\mathbf{v}}$ cannot be uniform among different fidelity levels due to the extraordinary cost of the physical experiment. It leads to the *heterotopic data* scenario, where some of the outputs from the physical environment are unavailable. Nonetheless, the derivation still holds with the heterotopic data, but the covariance matrix $\tilde{K}$ is inappropriate with matrix-wise calculation, as some elements in $K_\mathbf{P}$ of (17) correspond to un-examined data and will not be observed. Alternatively, if the number of data is n^j for the j-th data source, the matrix size will be changed, and $\tilde{K}$ becomes an $N \times N$ matrix, where $N = n^1 + n^2$. Each entry in $\tilde{K}$ can still be obtained by using (16) through element-wise calculation. Eqs. (18)-(20) will change accordingly, where $\tilde{k}(\mathbf{P}, \langle \mathbf{p}_t, j \rangle)$ becomes a vector of size $N \times 1$.

The MFBO approach can be outlined as a two-stage learning process, as summarized in **Algorithm 1**. First, we initialize a training data set by randomizing a set of parameter candidates $\mathbf{P}_{\text{init}}$ and measuring their output $\mathbf{v}_{\text{init}}$ through simulation. They construct the data set for the initial GP model training. Subsequently, by running the traditional BO on the simulation platform (with the fidelity identifier $j = 1$) in an iterative way, we generate an optimal parameter vector $\mathbf{p}^*_{j=1}$, along with the accumulation of data $[\langle \mathbf{p}_i, j = 1 \rangle, v_i]$. After that, we leverage $\mathbf{p}^*_{j=1}$ as the starting point and perform MFBO on the physical experiment platform (with the fidelity identifier $j = 2$). Following the evaluation of each candidate point $\mathbf{p}_k$, we augment the data set with a new tuple $\langle \mathbf{p}_k, j = 2 \rangle$ and its corresponding result v_k. The optimal parameter $\mathbf{p}^*_{j=2}$ is determined upon the completion of iterations in the MFBO process.

Importantly, by using the MFBO approach in Lines 12-23, the amount of information gained from both sources with different fidelities can be used and contribute to the optimization process on the real robot, which saves a significant overhead by avoiding re-exploring the same parameter space on the physical platform. Owing to the computational efficiency and accuracy of the simulation platform, our MFBO approach yields substantial improvements in terms of the speed of optimization.

5. System Architecture Overview

To run the MFBO algorithm on the physical robot, the algorithm requires either real-time access to the robot simulation model or the storage of the training data for solving the BO problem of (15). Either is a big challenge to the training efficiency and the real-time control of the physical robot. To alleviate the data storage and computational burden on the robot's onboard microprocessor, we employ an edge computing framework to offload the MFBO training process to an edge server.

The control system architecture of the soft quadruped robot is illustrated in Figure 3. The robot's onboard computation task mainly focuses on the sensor data collection and control signal actuation. This corresponds to a low level of decentralization (sometimes referred to as a distributed I/O approach). Three types of sensors are integrated into the robot, including the Inertial Measurement Unit (IMU), Time of Flight (ToF), and force sensors. Given the study's emphasis on walking speed, both IMU and ToF sensors are employed to estimate longitudinal velocity, while force sensors only contribute to footfall pattern analysis. The onboard collected data from the sensors are sent to the edge server

8

Algorithm 1: Multi-fidelity Bayesian optimization

Data: Initial set $\mathbf{P}_{\text{init}}$, design space bounds $[\underline{\mathbf{p}_i}, \overline{\mathbf{p}_i}]$, initial guess of K_f, number of iterations $i_{\max}$, $k_{\max}$, $i = k = 1$

Result: Optimal parameter on real robot $\mathbf{p}^*_{j=2}$

1   Evaluate $\mathbf{P}_{\text{init}}$ on the simulator and get $\mathbf{v}_{\text{init}}$;

2   Build $\mathcal{T} \leftarrow \{[\langle \mathbf{p}_i, j = 1 \rangle, v_i] \mid \mathbf{p}_i \in \mathbf{P}_{\text{init}}, v_i \in \mathbf{v}_{\text{init}}\}$;

3   Train GP model $g(\cdot)$ from $\mathcal{T}$ with parameter $\boldsymbol{\lambda}$;

4   **while** $i < i_{\max}$ **do**

5   Perform BO based on $\mathcal{T}$ and $\boldsymbol{\lambda}$, get new candidate point $\mathbf{p}_i$;

6   Evaluate $\mathbf{p}_i$ on the simulator and get v_i;

7   Update set: $\mathcal{T} \leftarrow \mathcal{T} \bigcup \{[\langle \mathbf{p}_i, j = 1 \rangle, v_i]\}$;

8   Update the GP model $g(\cdot)$ and get a new $\boldsymbol{\lambda}$;

9   Update iteration: $i \leftarrow i + 1$;

10 **end**

11 $\mathbf{p}^*_{j=1} \leftarrow \mathbf{p}_i, i = \arg\max_i(v_i), [\langle \mathbf{p}_i, j = 1 \rangle, v_i] \in \mathcal{T}$;

12 **while** $k < k_{\max}$ **do**

13   **if** $k = 1$ **then**

14          $\mathbf{p}_k = \mathbf{p}^*_{j=1}, \Lambda = \begin{bmatrix} \boldsymbol{\lambda} & \text{vec}(K_f) \end{bmatrix}^\top$

15   **else**

16   Perform MFBO based on $\mathcal{T}$ and Λ, get a new candidate point $\mathbf{p}_k$;

17   **end**

18   Evaluate $J(\mathbf{p}_k)$ on the real robot and get v_k;

19   Update set: $\mathcal{T} \leftarrow \mathcal{T} \bigcup \{[\langle \mathbf{p}_k, j = 2 \rangle, v_k]\}$;

20   Update the MTGP model $\tilde{g}(\cdot)$ and get a new Λ;

21   Update iteration: $k \leftarrow k + 1$;

22 **end**

23 $\mathbf{p}^* \leftarrow \mathbf{p}_k, k = \arg\max_k(v_k), [\langle \mathbf{p}_k, j = 2 \rangle, v_k] \in \mathcal{T}$;
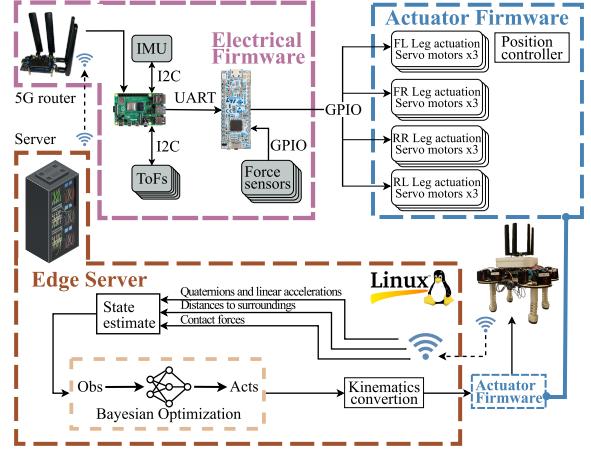

Figure 3: Control system architecture. The actuator and electrical firmware are physically integrated into the robot. The unidirectional arrows surrounding radio waves denote the transmission and reception of messages between soft robots and the edge server.

a Kalman filter. The resultant stabilized speed signal serves as the input for MFBO training, facilitating the optimization of parameters for the CPG controller. Subsequently, the oscillator signal is updated, and actuation commands are derived through kinematics conversion. The communication infrastructure between the robot's controller and the edge server relies on 5G technology, facilitated by the Quectel RM500Q-GL 5G HAT integrated into the soft robot. The employment of 5G communication not only provides improved reliability and lower latency for the real-time control task, but also enhances the mobility support with expanded coverage, which makes it particularly advantageous for potential industrial IoT use cases with the soft robots.

6. Results and Validation

6.1. Baseline Selection

To assess the effectiveness of the implemented BO approach during the training phase, we conduct performance comparisons with the following baselines. These baselines include algorithms/search methods previously introduced in Sec. 1, which serve as a reference for state-of-the-art approaches in the domain.

- Adaptive grid search (AGS) [49]: Owing to the exponential complexity associated with grid search at a finer granularity for sampling, an Adaptive Grid Search (AGS) approach is used to avoid exhaustive search. AGS iteratively refines the search space based on promising regions from the previous optimal solution. We consider the point identified by AGS as the global optimum.

for the state estimation of the robot's velocity. Subsequently, the robot receives control signals from the edge server to govern soft leg actuation. Actuation is executed through position control of the servo motors, with lower-level PD controllers enhancing stability and efficiency.

The edge server is dedicated to executing computationally and memory-intensive tasks, encompassing functions such as state estimation, MFBO training, CPG oscillator calculation, and kinematics conversion. All functionalities on the edge server are deployed within a virtual machine operating in the Ubuntu 20.04 environment. The raw data of sensor feedback from the soft quadruped robot, including quaternions and linear accelerations, distances to surroundings, and contact forces, are fused to enhance speed estimation through

- Simulated annealing (SA) [50]: SA is utilized as the benchmark for black-box optimization comparison due to its effectiveness as a single-point search algorithm. Note that population-based algorithms, e.g., Genetic Algorithms (GA) [37] and Particle Swarm Optimization (PSO), are not ideal due to the computational expense of evaluating a substantial amount of samples per iteration.

- Random search (RS) [51]: RS represents a worst-case scenario without intelligent exploration, which is used to quantify the improvement of the other methods.

- Omni-directional walking design (OWD) [8]: OWD is proposed in the previous work for the soft robot walking gait design. It is regarded as a baseline in terms of ad hoc design without optimization or search processes; thus, it is only used to compare the performance of the identified optimal gait pattern.

Note that, except OWD, the other baselines are solely employed for evaluating the optimization performance at the simulation level, as they cannot effectively control the physical robot to walk. Except AGS, each search method is assessed through 3 evaluations using distinct random seeds. We impose a predefined limit of 300 iterations as a stopping criterion for SA, RS, and BO.

The selection of the surrogate model in BO is crucial in identifying optimal points of design parameters. As commented in Sec. 2.2, various surrogate models may be employed for BO. Specifically, we assess the performance of these surrogate models against GP, which are summarized and outlined in a previous study [45]:

- Random forest (RF) [52]: RF is an ensemble method consisting of multiple regression trees. Each tree is trained on a bootstrap sample of the training data, and the final prediction is obtained by averaging the predictions of all trees.

- Random Fourier Expansion (RFE) [53]: RFE generates random features using Fourier basis functions and trains a linear regression model on these features to approximate the objective function.

- Support Vector Machine (SVM) [54]: SVM finds the best hyperplane to separate different classes by maximizing the margin between support vectors. We use Radial Basis Function (RBF) as the kernel function.

Table 1: Comparison of the optimization performance

	ADS	SA	RS	BO
Max speed (m/s)	0.312	0.264	0.125	0.286
Optimization time (h)	72.367	5.025	4.567	1.278

- Piece-wise Linear (PL) [55]: PL surrogate model uses rectified linear units (ReLUs) in a linear combination, where the ReLU input represents the linear mapping of the input data [55].

The hyperparameters in the surrogate models are configured in alignment with the studies referenced by Bliek et al. [45]. All the simulation evaluations are executed on a desktop with Intel(R) Core(TM) i7-8700 CPU at 3.20 GHz, six cores, and 8.0 GB installed memory (RAM).

6.2. Comparison of Optimization Methods

Table 1 lists the optimization results by different methods with the associated computational time. Note that this comparison is conducted with the simulation platform. Among all the methods, ADS delivers the best performance with the global optimum speed at 0.312 m/s. Nevertheless, it comes at a significant computational time cost, consuming over 72 hours as it evaluated 3072 points within 3 iteratively refined parameter regions. In contrast, the BO approach only takes 1.278 hours to converge after roughly 70 iterations, reaching an optimal speed of 0.286 m/s, which corresponds to 91.67% of the global optimum. In addition, SA does not meet the objective function tolerance criteria and gets terminated at 300 rounds. It results in an identified optimal point of 0.264 m/s in a duration of 5.025 hours, which is slightly worse than BO. On the other hand, RS provides a lower bound reference of employing the defined CPG oscillator-based gait pattern. It offers a baseline speed of 0.125 m/s and consumes 4.567 hours to finish the 300-iteration search. In comparison to ADS and RS, the application of the BO approach demonstrates its effectiveness in exploring the optimal gait pattern for soft robots. Additionally, in the context of black-box optimization, it also exhibits superior efficiency compared to SA. Moreover, the underlying GP model in BO facilitates domain adaptation for subsequent sim-to-real transfer, which is a feature not achievable by SA.

For a more comprehensive analysis of the robustness of BO, Figure 4 illustrates the BO training performance across different trials with randomly initialized seeds and noise, where the corresponding parameter setting is given in Table 3. Note that the variable ranges are

10

defined with the same extreme values as deployed in the study [8] for a fair comparison. It can be seen that the robot stays at an exploration phase within the design space for the first 40 iterations, followed by a noticeable performance improvement for the next 20 iterations. Subsequently, convergence is achieved with a stable speed at around 70 iterations. In the simulated environment, the robot ultimately learns a stable speed of approximately 0.28 m/s. This represents a remarkable improvement compared with the previous study [8] (0.14 m/s). The optimized gait pattern **s** within the identical motion space leads to a twofold increase in walking speed.

6.3. Comparison of Surrogate Models

Table 2 compares the performance of different surrogate models. We construct a test data set by pseudo-randomly selecting 1000 samples in order to cover the entire design search space. We evaluate goodness-of-fit of models with R^2 and NMSE to quantify the prediction accuracy. To evaluate the generalization and robustness of the model, we conduct the experiments through a 5-fold *cross-validation* by partitioning the dataset into five subsets, using each subset once as a validation set, and averaging the performance metrics across all folds. Hence, we present the mean R^2 and its standard deviation from cross-validation, along with the mean NMSE. In addition, we evaluate the computational time for each surrogate model regression to assess their computational complexity.

In Table 2, it is evident that under a relatively small dataset scenario, the employed GP surrogate model exhibits a noticeable advantage over other methods in terms of modeling accuracy. Furthermore, during the cross-validation experiment, it demonstrates the lowest standard deviation value, indicating stable out-of-sample performance and strong generalization to unseen data. On the other hand, the GP method has larger computational complexities, which grow cubically and quadratically with the number of training points during model training and online inference, respectively. In comparison to other benchmark methods, it only shows better computational efficiency against PL, which requires back-propagating training for ReLUs. This result gives us insights into the trade-off between model accuracy and real-time efficiency when employing the GP model, thereby emphasizing the significance and justification of our edge off-loading architecture.

6.4. MFBO and Physical Deployment

This section addresses the results of MFBO during the physical deployment, and the training process is de-

Table 2: Cross-validation for comparing the surrogate models

	RF	RFE	SVM	PL	GP
Mean R^2	0.9373	0.8880	0.8902	0.9294	0.9856
Standard deviation	0.0121	0.0262	0.0220	0.0140	0.0049
Mean NMSE	0.1134	0.1519	0.1487	0.1201	0.0478
Computational time (s)	0.0546	0.1584	0.1180	10.9937	4.7888

Table 3: Parameter setting for BO training

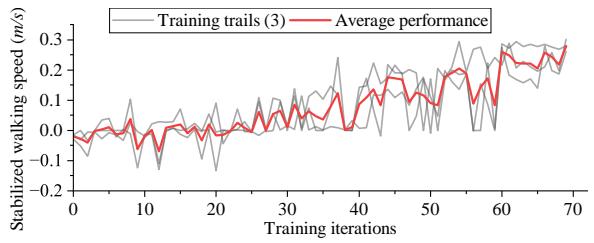| Parameters	Values
$\mid \mathbf{P}_{\text{init}} \mid$	10
$\bar{\mathbf{p}}$	$[0.7, 0.008, 2, 0.9, 2\pi]^\top$
$\underline{\mathbf{p}}$	$[0.1, 0.001, 0.4, 0.1, 0]^\top$
i_{max}	70

Figure 4: BO training on simulation platform

picted in Figure 5. As previously noted, we initiated the MFBO training with the optimal gait discovered in the simulation environment. Due to model errors, the robot's actual walking behavior differs from the simulated speed. Specifically, it struggles to attain the desired speed and only reaches approximately 0.025m/s[1]. Nevertheless, after several iterations of MFBO training, the robot rapidly adjusts the walking pattern to suit the physical environment. Consequently, its walking speed gradually increases to around 0.2 m/s and reaches a saturation point. Despite some oscillations and fluctuations in the training curves across 5 different trials attributable to environmental noise, they exhibit a consistent overall trend and stabilize within 10 iterations.

Furthermore, the robot's walking speed at the optimized point in the physical environment is plotted in Figure 6. As before, we conduct 5 trials and provide both individual trial results and the average performance. The robot accelerates to a stable speed with approximately 1.2 s. In particular, the largest speed goes up to 0.344 m/s during the testing with an average stabilized speed of 0.214 m/s. This represents a significant improvement of 52.71% compared to the physical testing results of the OWD solution within the same param-

---

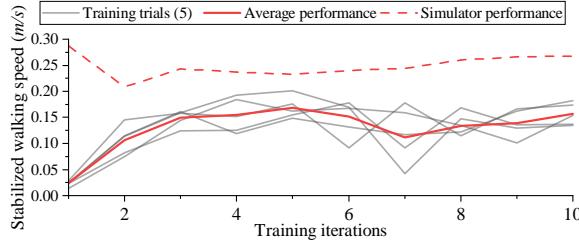[1]The corresponding motion patterns are viewable in the attached video.
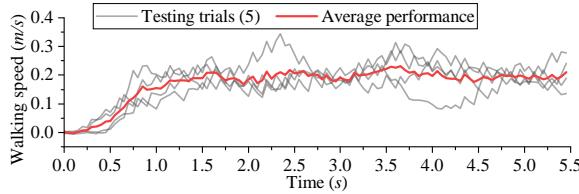
Figure 5: MFBO physical training

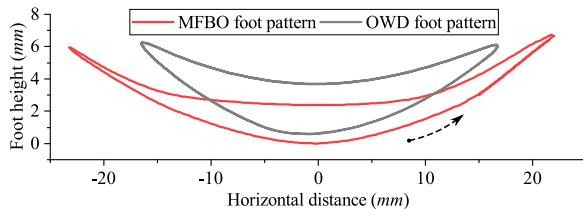Figure 6: Walking test of the optimized parameters.

Figure 7: Comparison of the foot pattern.

(a) $t = 0\ s$ (b) $t = 2.5\ s$
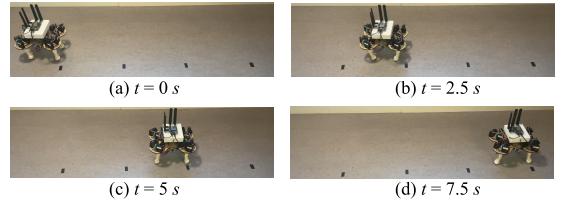(c) $t = 5\ s$ (d) $t = 7.5\ s$

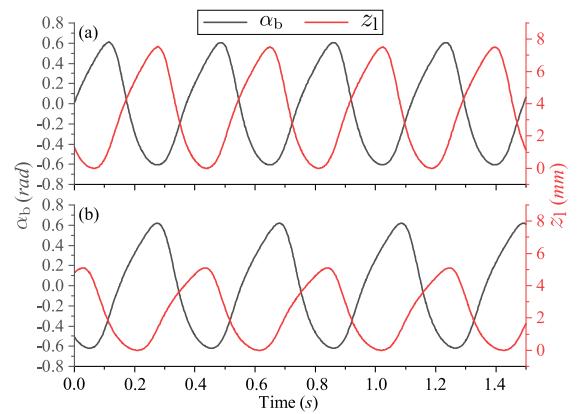Figure 8: Physical test results of the converged motion pattern captured in video frames.

Figure 9: Comparison of behaviors of optimized oscillators. (a): Simulation platform, (b): Physical testing platform.

eter range. Figure 8 shows the physical test results of the converged motion pattern[1].

Figure 7 plots and compares the foot trajectories between the MFBO and OWD gaits. The MFBO controller demonstrates a substantially increased swing distance in the direction of motion, resulting in an approximately twofold expansion of the horizontal distance compared to the OWD foot pattern. In addition, both foot patterns attain a similar maximal foot height. Note that the design space of the leg's state $\mathbf{s}$ remains consistent across both methods. However, the swing trajectories of α_b and z_l are different for two methods during the design phase. This disparity leads to distinct phase synchronization behaviors between α_b and z_l, influencing the maximal horizontal distances and subsequently impacting walking patterns and speeds.

In addition, as shown in Figure 9, a comparison of oscillator behaviors is made between the optimal point identified in the simulator and the physical environment. According to (14), the oscillator exhibits varying characteristics depending on the design parameter vector $\mathbf{p}$. Relative to the optimized gait observed in the simulator, the oscillator associated with the optimal gait

in the physical test exhibits a comparatively lower frequency value f and a higher value for the shape ratio α. These differences suggest a more prompt transition between the two swing phases during physical training. The maximal bending angle α_b remains consistent across both data sources; however, in the physical testing scenario, the robot's leg requires less time for the swing-back motion and tends to exert a greater force during the rearward push against the ground. This phenomenon corresponds to the previously discussed reality gap in Figure 5, as the robot encounters challenges in generating sufficient power to facilitate forward movement when operating with the optimal gait derived from the simulator. Consequently, it shows more aggressive behavior by shortening the duration of the swing-back phase. Moreover, in Figure 9(b), z_l exhibits a noticeable decrease accordingly, which is inferred to compensate for the alteration in α, since keeping the same amount of z_l with a larger α will challenge the motor response capacity. Also, increasing α without decreasing z_l will result in an overly aggressive gait pattern, potentially leading to kinetic friction and causing slippage.

12

6.5. Off-loading performance comparison

To highlight the necessity of edge computing architecture to realize the task off-loading process, we conducted a comparative analysis of CPG calculations executed on the robot's control board and the edge server. Note that the MFBO training part is exclusively offloaded to the edge server and is not considered in this comparison due to its excessive computational resource demands on the robot's board. Owing to the contention of computational resource in a multi-thread setup, control tasks on the robot's onboard controller may become overdue, resulting in missed deadlines. Therefore, we evaluate the overdue status of the control tasks.

As shown in Figure 10(a), when the control task is offloaded, the computation of the CPG actuation signals is accelerated by leveraging the advanced computation capacity of the edge server. In this scenario, 5G communication contributes to a larger portion of the total delay, which is primarily limited by the fixed proximity of the edge server and 5G bandwidth availability. The resulting end-to-end latency satisfies the defined control frequency (20 Hz), thus enabling a smooth gait actuation in the physical deployment, with average and maximum delays 28.215 *ms* and 42.779 *ms*, respectively. Conversely, executing the computation task on the onboard controller leads to longer execution time delays, and some jobs miss the deadline. We profile the overload of the onboard computation from a thread in the lower-level controller in Figure 10(b) and evaluate the performance influence. It is noteworthy that the plotted time consumption in Figure 10(b) exclusively reflects the execution of the control task. However, some instances of missed deadlines, as observed in the figure, occur despite computation delays below 50 *ms*. This phenomenon is attributed to the incomplete execution of perception and actuation tasks within the closed-loop control period. Thus, the degradation in real-time performance results in an inconsistent and incoherent gait pattern, with the robot getting stuck in certain postures due to missed actuation signals[2].

6.6. Domain Adaptation and Reality Gap

As discussed in Sec. 4.2, the domain adaptation of MFBO is realized by determining the matrix K_f with physical experiments, and it represents the correlation between the simulator and the physical robot. To increase its interpretability, a transformation is performed on K_f by *diagonal elements normalization* [56].
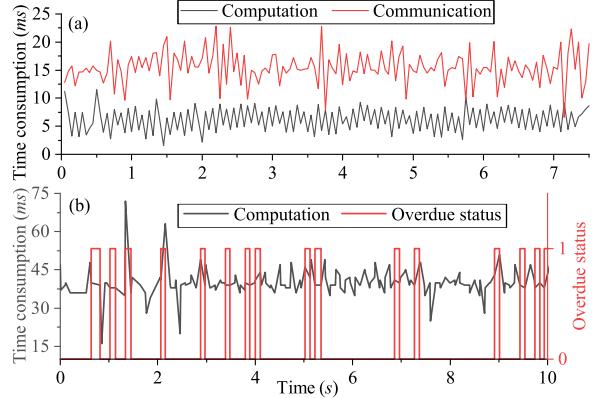

Figure 10: Comparison of the time consumption of real-time control when the CPG is calculated at (a): edge server, (b): robot's onboard controller.

We refer to the normalized matrix as K'_f, and $K'_f = \begin{bmatrix} 1 & 0.575 \\ 0.575 & 1 \end{bmatrix}$. The diagonal elements of K'_f are unit values to eliminate the influence of label-specific scaling. The off-diagonal elements indicate that the dynamic properties of the simulator and the robot have a moderately positive correlation.

In addition, we perform a bi-directional comparison to verify the reality gap, where the performance of the optimized parameters in different MFBO iterations from a training trail is cross-validated in the simulator. The corresponding velocities are plotted in Figure 5. Notably, in the simulated platform's initial iteration, the robot achieves its maximum velocity despite exhibiting the worst physical performance. Subsequently, the velocities in the simulator drops and gets stabilized for the other candidate points as the MFBO physical training progresses. Nevertheless, it consistently maintains a higher velocity than that observed in the physical realization. The cross-validation verifies the non-linear correlation of the addressed objective function across different data sources. Based on the simulation results, the *Pearson's correlation coefficient* is calculated with $K_{bi} = \begin{bmatrix} 1 & 0.601 \\ 0.601 & 1 \end{bmatrix}$. The high consistency between K_{bi} and K_f verifies that our estimated model has a high accuracy for domain adaptation, which leads to the realization of the MFBO with high efficiency.

7. Conclusion and Future Work

This study investigates advanced gait pattern design for a tendon-driven soft quadruped robot, with a specific focus on bridging the reality gap mitigation through

---

[2]The comparison of real-time control performance is shown in the video attachment.

learning-enhanced methods. The gait design exploits a parametric model based on Central Pattern Generators (CPG) with Hopf oscillators, whose parameters are determined through Bayesian Optimization (BO) using both simulation and experimental data. Furthermore, to ensure a smooth sim-to-real transfer, we refine the BO method and propose a multi-fidelity Bayesian Optimization (MFBO) approach for domain adaptation, thus efficiently compensating for modeling errors and overcoming the reality gap. Moreover, the entire training process utilizes an edge computing off-loading scheme with 5G communication, enhancing real-time data collection, training, control performance, and potential industrial applications. Future work includes investigation into walking properties for optimization and exploration of high-level navigation tasks on the soft quadruped robot platform. In addition, the communication dependence introduced by the off-loading scheme raises potential vulnerability due to communication loss. Hence, future work could extend this study by developing methods to enable the system to continue operation in a degraded mode and transition into a fail-safe state.

Declaration of competing interest

The authors declare that they have no known competing financial interests or personal relationships that could have appeared to influence the work reported in this paper.

Declaration of generative AI and AI-assisted technologies in the writing process

During the preparation of this work the author(s) used ChatGPT in order to improve readability and language of the work. After using this tool/service, the author(s) reviewed and edited the content as needed and take(s) full responsibility for the content of the publication.

Acknowledgements

CRediT authorship contribution statement

Kaige Tan: Conceptualization, Methodology, Software, Validation, Formal analysis, Investigation, Writing Original Draft, Visualization. **Xuezhi Niu, Qinglei Ji:** Methodology, Software, Investigation. **Lei Feng, Martin Törngren:** Supervision, Project administration, Funding acquisition, Writing-Review & Editing.

References

[1] O. Yasa, Y. Toshimitsu, M. Y. Michelis, L. S. Jones, M. Filippi, T. Buchner, R. K. Katzschmann, An overview of soft robotics, Annual Review of Control, Robotics, and Autonomous Systems 6 (2023) 1–29. doi:10.1146/annurev-control-062322-100607.

[2] R. S. Diteesawat, T. Helps, M. Taghavi, J. Rossiter, Electropneumatic pumps for soft robotics, Science robotics 6 (51) (2021) eabc3721. doi:10.1126/scirobotics.abc3721.

[3] K. Tan, Q. Ji, L. Feng, M. Törngren, Shape estimation of a 3D printed soft sensor using multi-hypothesis extended Kalman filter, IEEE Robotics and Automation Letters 7 (3) (2022) 8383–8390. doi:10.1109/LRA.2022.3187832.

[4] Z. Ma, D. Sameoto, A review of electrically driven soft actuators for soft robotics, Micromachines 13 (11) (2022) 1881. doi:10.3390/mi13111881.

[5] Q. Ji, S. Fu, K. Tan, S. T. Muralidharan, K. Lagrelius, D. Danelia, G. Andrikopoulos, X. V. Wang, L. Wang, L. Feng, Synthesizing the optimal gait of a quadruped robot with soft actuators using deep reinforcement learning, Robotics and Computer-Integrated Manufacturing 78 (2022) 102382. doi:10.1016/j.rcim.2022.102382.

[6] N. Ebrahimi, C. Bi, D. J. Cappelleri, G. Ciuti, A. T. Conn, D. Faivre, N. Habibi, A. Hošovský, V. Iacovacci, I. S. Khalil, et al., Magnetic actuation methods in bio/soft robotics, Advanced Functional Materials 31 (11) (2021) 2005137. doi:10.1002/adfm.202005137.

[7] Y. Dong, L. Wang, N. Xia, Z. Yang, C. Zhang, C. Pan, D. Jin, J. Zhang, C. Majidi, L. Zhang, Untethered small-scale magnetic soft robot with programmable magnetization and integrated multifunctional modules, Science advances 8 (25) (2022) eabn8932. doi:10.1126/sciadv.abn8932.

[8] Q. Ji, S. Fu, L. Feng, G. Andrikopoulos, X. V. Wang, L. Wang, Omnidirectional walking of a quadruped robot enabled by compressible tendon-driven soft actuators, in: 2022 IEEE/RSJ International Conference on Intelligent Robots and Systems (IROS), IEEE, 2022, pp. 11015–11022. doi:10.1109/IROS47612.2022.9981314.

[9] D. Drotman, S. Jadhav, D. Sharp, C. Chan, M. T. Tolley, Electronics-free pneumatic circuits for controlling soft-legged robots, Science Robotics 6 (51) (2021) eaay2627. doi:10.1126/scirobotics.aay2627.

[10] K. Tan, Q. Ji, L. Feng, M. Törngren, Edge-enabled adaptive shape estimation of 3D printed soft actuators with Gaussian processes and unscented Kalman filters, IEEE Transactions on Industrial Electronics 71 (3) (2024) 3044–3054. doi:10.1109/TIE.2023.3270505.

[11] W.-L. Ma, K. A. Hamed, A. D. Ames, First steps towards full model based motion planning and control of quadrupeds: A hybrid zero dynamics approach, in: 2019 IEEE/RSJ International Conference on Intelligent Robots and Systems (IROS),

IEEE, 2019, pp. 5498–5503. `doi:10.1109/IROS40897. 2019.8968189`.

[12] P. M. Wensing, M. Posa, Y. Hu, A. Escande, N. Mansard, A. Del Prete, Optimization-based control for dynamic legged robots, IEEE Transactions on Robotics 40 (2024) 43–63. `doi: 10.1109/TRO.2023.3324580`.

[13] J. M. Bern, P. Banzet, R. Poranne, S. Coros, Trajectory optimization for cable-driven soft robot locomotion., in: Robotics: Science and Systems, 2019, pp. 1–8.

[14] C. Della Santina, C. Duriez, D. Rus, Model-based control of soft robots: A survey of the state of the art and open challenges, IEEE Control Systems Magazine 43 (3) (2023) 30–65. `doi: 10.1109/MCS.2023.3253419`.

[15] J. Ibarz, J. Tan, C. Finn, M. Kalakrishnan, P. Pastor, S. Levine, How to train your robot with deep reinforcement learning: lessons we have learned, The International Journal of Robotics Research 40 (4-5) (2021) 698–721. `doi:10.1177/ 0278364920987859`.

[16] T. Miki, J. Lee, J. Hwangbo, L. Wellhausen, V. Koltun, M. Hutter, Learning robust perceptive locomotion for quadrupedal robots in the wild, Science Robotics 7 (62) (2022) eabk2822. `doi:10.1126/scirobotics.abk2822`.

[17] H. Shi, B. Zhou, H. Zeng, F. Wang, Y. Dong, J. Li, K. Wang, H. Tian, M. Q.-H. Meng, Reinforcement learning with evolutionary trajectory generator: A general approach for quadrupedal locomotion, IEEE Robotics and Automation Letters 7 (2) (2022) 3085–3092. `doi:10.1109/LRA.2022. 3145495`.

[18] G. Lan, M. De Carlo, F. van Diggelen, J. M. Tomczak, D. M. Roijers, A. Eiben, Learning directed locomotion in modular robots with evolvable morphologies, Applied Soft Computing 111 (2021) 107688. `doi:10.1016/j.asoc.2021.107688`.

[19] G. Bellegarda, A. Ijspeert, CPG-RL: Learning central pattern generators for quadruped locomotion, IEEE Robotics and Automation Letters 7 (4) (2022) 12547–12554. `doi:10.1109/ LRA.2022.3218167`.

[20] Y. Zhang, M. Thor, N. Dilokthanakul, Z. Dai, P. Manoonpong, Hybrid learning mechanisms under a neural control network for various walking speed generation of a quadruped robot, Neural Networks 167 (2023) 292–308. `doi:10.1016/j.neunet. 2023.08.030`.

[21] Y. Ding, A. Pandala, C. Li, Y.-H. Shin, H.-W. Park, Representation-free model predictive control for dynamic motions in quadrupeds, IEEE Transactions on Robotics 37 (4) (2021) 1154–1171. `doi:10.1109/TRO.2020.3046415`.

[22] Y. Gao, W. Wei, X. Wang, D. Wang, Y. Li, Q. Yu, Trajectory tracking of multi-legged robot based on model predictive and sliding mode control, Information Sciences 606 (2022) 489–511. `doi:10.1016/j.ins.2022.05.069`.

[23] R. Grandia, F. Jenelten, S. Yang, F. Farshidian, M. Hutter, Perceptive locomotion through nonlinear model-predictive control, IEEE Transactions on Robotics 39 (5) (2023) 3402–3421. `doi:10.1109/TRO.2023.3275384`.

[24] H. Taheri, N. Mozayani, A study on quadruped mobile robots, Mechanism and Machine Theory 190 (2023) 105448. `doi:10. 1016/j.mechmachtheory.2023.105448`.

[25] S. Hürkey, N. Niemeyer, J.-H. Schleimer, S. Ryglewski, S. Schreiber, C. Duch, Gap junctions desynchronize a neural circuit to stabilize insect flight, Nature 618 (7963) (2023) 118–125. `doi:10.1038/s41586-023-06099-0`.

[26] Y. Shao, Y. Jin, X. Liu, W. He, H. Wang, W. Yang, Learning free gait transition for quadruped robots via phase-guided controller, IEEE Robotics and Automation Letters 7 (2) (2021) 1230–1237. `doi:10.1109/LRA.2021.3136645`.

[27] Z. Song, J. Zhu, J. Xu, Gaits generation of quadruped loco-

[28] G. Lan, M. De Carlo, F. van Diggelen, J. M. Tomczak, D. M. Roijers, A. E. Eiben, Learning directed locomotion in modular robots with evolvable morphologies, Applied Soft Computing 111 (2021) 107688. `doi:10.1016/j.asoc.2021.107688`.

[29] M. Okulewicz, M. Zaborski, J. Mańdziuk, Self-adapting particle swarm optimization for continuous black box optimization, Applied Soft Computing 131 (2022) 109722. `doi:10.1016/ j.asoc.2022.109722`.

[30] G. Nadizar, E. Medvet, S. Nichele, S. Pontes-Filho, An experimental comparison of evolved neural network models for controlling simulated modular soft robots, Applied Soft Computing 145 (2023) 110610. `doi:10.1016/j.asoc.2023.110610`.

[31] H. Jiang, T. Chen, J. Cao, J. Bi, G. Lu, G. Zhang, X. Rong, Y. Li, Stable skill improvement of quadruped robot based on privileged information and curriculum guidance, Robotics and Autonomous Systems 170 (2023) 104550. `doi:10.1016/j. robot.2023.104550`.

[32] P. Perdikaris, G. E. Karniadakis, Model inversion via multi-fidelity bayesian optimization: a new paradigm for parameter estimation in haemodynamics, and beyond, Journal of The Royal Society Interface 13 (118) (2016) 20151107. `doi:10. 1098/rsif.2015.1107`.

[33] A. Marco, F. Berkenkamp, P. Hennig, A. P. Schoellig, A. Krause, S. Schaal, S. Trimpe, Virtual vs. real: Trading off simulations and physical experiments in reinforcement learning with bayesian optimization, in: 2017 IEEE International Conference on Robotics and Automation (ICRA), IEEE, 2017, pp. 1557–1563. `doi:10.1109/ICRA.2017.7989186`.

[34] T. Wei, S. Wang, J. Zhong, D. Liu, J. Zhang, A review on evolutionary multitask optimization: Trends and challenges, IEEE Transactions on Evolutionary Computation 26 (5) (2022) 941–960. `doi:10.1109/TEVC.2021.3139437`.

[35] Y. Zhang, Q. Yang, A survey on multi-task learning, IEEE Transactions on Knowledge and Data Engineering 34 (12) (2022) 5586–5609. `doi:10.1109/TKDE.2021.3070203`.

[36] S. Horváth, A. Klein, P. Richtarik, C. Archambeau, Hyperparameter transfer learning with adaptive complexity, in: A. Banerjee, K. Fukumizu (Eds.), Proceedings of the 24th International Conference on Artificial Intelligence and Statistics, Vol. 130 of Proceedings of Machine Learning Research, PMLR, 2021, pp. 1378–1386.

[37] H. Wang, Y. Jin, C. Yang, L. Jiao, Transfer stacking from low-to high-fidelity: A surrogate-assisted bi-fidelity evolutionary algorithm, Applied soft computing 92 (2020) 106276. `doi: 10.1016/j.asoc.2020.106276`.

[38] E. Lau, V. Srivastava, S. D. Bopardikar, A multi-fidelity bayesian approach to safe controller design, IEEE Control Systems Letters 7 (2023) 2904–2909. `doi:10.1109/LCSYS. 2023.3290475`.

[39] M. G. Fernández-Godino, Review of multi-fidelity models, Advances in Computational Science and Engineering 1 (4) (2023) 351–400. `doi:10.3934/acse.2023015`.

[40] J. M. G. Sánchez, N. Jörgensen, M. Törngren, R. Inam, A. Berezovskyi, L. Feng, E. Fersman, M. R. Ramli, K. Tan, Edge computing for cyber-physical systems: A systematic mapping study emphasizing trustworthiness, ACM Transactions on Cyber-Physical Systems (TCPS) 6 (3) (2022) 1–28. `doi:10. 1145/3539662`.

[41] M. Groshev, G. Baldoni, L. Cominardi, A. de la Oliva, R. Gazda, Edge robotics: Are we ready? An experimental evaluation of current vision and future directions, Digital Communications and Networks 9 (1) (2023) 166–174. `doi:10.1016/j.dcan.`

2022.04.032.

[42] J. Yang, Y. Wang, Z. Li, Inverse order based optimization method for task offloading and resource allocation in mobile edge computing, Applied Soft Computing 116 (2022) 108361. `doi:10.1016/j.asoc.2021.108361`.

[43] K. Tan, L. Feng, G. Dán, M. Törngren, Decentralized convex optimization for joint task offloading and resource allocation of vehicular edge computing systems, IEEE Transactions on Vehicular Technology 71 (12) (2022) 13226–13241.

[44] T. Qiu, J. Chi, X. Zhou, Z. Ning, M. Atiquzzaman, D. O. Wu, Edge computing in industrial internet of things: Architecture, advances and challenges, IEEE Communications Surveys & Tutorials 22 (4) (2020) 2462–2488. `doi:10.1109/COMST.2020.3009103`.

[45] L. Bliek, A. Guijt, R. Karlsson, S. Verwer, M. de Weerdt, Benchmarking surrogate-based optimisation algorithms on expensive black-box functions, Applied Soft Computing 147 (2023) 110744. `doi:10.1016/j.asoc.2023.110744`.

[46] J. Snoek, H. Larochelle, R. P. Adams, Practical bayesian optimization of machine learning algorithms, in: Advances in Neural Information Processing Systems, Vol. 25, Curran Associates, Inc., 2012, pp. 1–9.

[47] C. Zhou, K. Low, Design and locomotion control of a biomimetic underwater vehicle with fin propulsion, IEEE/ASME Transactions on Mechatronics 17 (1) (2011) 25–35. `doi:10.1109/TMECH.2011.2175004`.

[48] M. A. Álvarez, L. Rosasco, N. D. Lawrence, Kernels for vector-valued functions: A review, Foundations and Trends® in Machine Learning 4 (3) (2012) 195–266. `doi:10.1561/2200000036`.

[49] Y. Shi, G. Zhao, M. Wang, Y. Xu, An adaptive grid search algorithm for fitting spherical target of terrestrial LiDAR, Measurement 198 (2022) 111430. `doi:10.1016/j.measurement.2022.111430`.

[50] D. Delahaye, S. Chaimatanan, M. Mongeau, Simulated annealing: From basics to applications, Handbook of metaheuristics (2019) 1–35 `doi:10.1007/978-3-319-91086-4{\_}1`.

[51] S. Andradóttir, An overview of simulation optimization via random search, Handbooks in operations research and management science 13 (2006) 617–631. `doi:10.1016/S0927-0507(06)13020-0`.

[52] F. Hutter, H. H. Hoos, K. Leyton-Brown, Sequential model-based optimization for general algorithm configuration, in: Learning and Intelligent Optimization: 5th International Conference, LION 5, Rome, Italy, January 17-21, 2011. Selected Papers 5, Springer, 2011, pp. 507–523. `doi:10.1007/978-3-642-25566-3{\_}40`.

[53] L. Bliek, H. R. Verstraete, M. Verhaegen, S. Wahls, Online optimization with costly and noisy measurements using random fourier expansions, IEEE transactions on neural networks and learning systems 29 (1) (2016) 167–182. `doi:10.1109/TNNLS.2016.2615134`.

[54] P. Saves, R. Lafage, N. Bartoli, Y. Diouane, J. Bussemaker, T. Lefebvre, J. T. Hwang, J. Morlier, J. R. Martins, Smt 2.0: A surrogate modeling toolbox with a focus on hierarchical and mixed variables gaussian processes, Advances in Engineering Software 188 (2024) 103571. `doi:10.1016/j.advengsoft.2023.103571`.

[55] L. Bliek, S. Verwer, M. de Weerdt, Black-box combinatorial optimization using models with integer-valued minima, Annals of Mathematics and Artificial Intelligence 89 (7) (2021) 639–653. `doi:10.1007/s10472-020-09712-4`.

[56] R. Dürichen, M. A. Pimentel, L. Clifton, A. Schweikard, D. A. Clifton, Multitask Gaussian processes for multivariate physiological time-series analysis, IEEE Transactions on Biomedical Engineering 62 (1) (2014) 314–322. `doi:10.1109/TBME.2014.2351376`.